# Negative-band-gap quantum dots: Gap collapse, intrinsic surface states, excitonic response, and excitonic insulator phase

Natalia Malkova* and Garnett W. Bryant

*Atomic Physics Division and Joint Quantum Institute, National Institute of Standards and Technology, Gaithersburg, Maryland 20899-8423, USA*

(Received 11 June 2010; revised manuscript received 23 September 2010; published 18 October 2010)

The spectrum of quantum dots made from semiconductors such as HgTe and HgS changes from negative gap to positive gap with decreasing size. Furthermore, intrinsic surface states, which are not related to dangling bonds, appear in the negative-gap regime. We investigate theoretically the evolution of the spectrum of HgS quantum dots with decreasing size and show how states evolve from a negative gap to a positive gap as confinement is increased. The lowest confined electron level evolves into an intrinsic surface state with increasing size and, thus, is not derived directly from a bulk HgS band. Due to strong band mixing in narrow-gap semiconductors, spacing between confined levels decreases more slowly with increasing size than for quantum dots made from wide-gap semiconductors. Moreover, dielectric screening becomes nearly metallic as the gap closes. As a consequence, confinement energies dominate exciton binding energies for all dot sizes up to the gap closure. Excitons remain in the strong confinement limit as size increases until the gap closes. Nonetheless, the exciton binding exceeds the single-particle gap for sizes near gap closure, opening up the possibility of an excitonic insulator phase in quantum dots not possible in positive-gap quantum dots. Signatures in the quantum-dot optical response for gap collapse and surface states are identified.

DOI: 10.1103/PhysRevB.82.155314 PACS number(s): 73.21.La, 78.66.Hf, 73.20.At, 71.35.−y

## I. INTRODUCTION

Quantum dots (QDs) made from negative-bulk-band-gap materials, including HgTe, HgSe, and $\beta$-HgS (the zinc-blende phase of HgS), have a broad range of possible technological applications that could be exploited and fundamental issues that should be addressed. For example, negative-bulk-band-gap materials are gapless semiconductors or semimetals. When confined as QDs, they should exhibit small positive band gaps, that can be controlled by the dot size. These tunable small gaps make these QDs ideal for applications as nanodetectors and nanosensors in the far infrared.[1,2] For QDs with energy gaps close to the gapless state, the exciton binding energy may become larger than the energy gap, opening up the possibility of an "excitonic insulator" phase in QDs.[3] In this case, the normal insulating ground state with a filled valence band would become unstable against formation of electron-hole pairs. Moreover, it has been proposed recently that such gapless materials will manifest a topological insulator phase that makes them attractive for applications in quantum computing and spintronics.[4] An understanding for the evolution of quantum confinement effects in QDs made from negative-gap materials is needed to pursue applications and assess possible new phases in QDs.

Understanding quantum confinement, excitonic states, and optical response in negative-band-gap nanocrystals provides challenges not posed for nanocrystals made from positive-band-gap semiconductors, such as CdTe, CdSe, and CdS. These positive-band-gap semiconductors have a direct band structure, with the $s$-type $\Gamma_6$ band lying above the $p$-type $\Gamma_8$ band and the bulk band gap $E_g^b = E_{\Gamma_6} - E_{\Gamma_8} > 0$, as shown in the upper panel of Fig. 1. The band gap $E_g^d$ of QDs made of positive-gap semiconductors with parabolic dispersion roughly follows the normal (particle in a box) confinement so that $E_g^d \approx E_g^b + \hbar^2\pi^2/(2R^2)(1/m_e + 1/m_h)$ (where $m_{e,h}$ are the electron and hole effective masses and $R$ is the QD radius). Although there is some controversial data on the band arrangement in negative band-gap materials,[5–7] most experiments[8–12] demonstrate that these materials have an in-

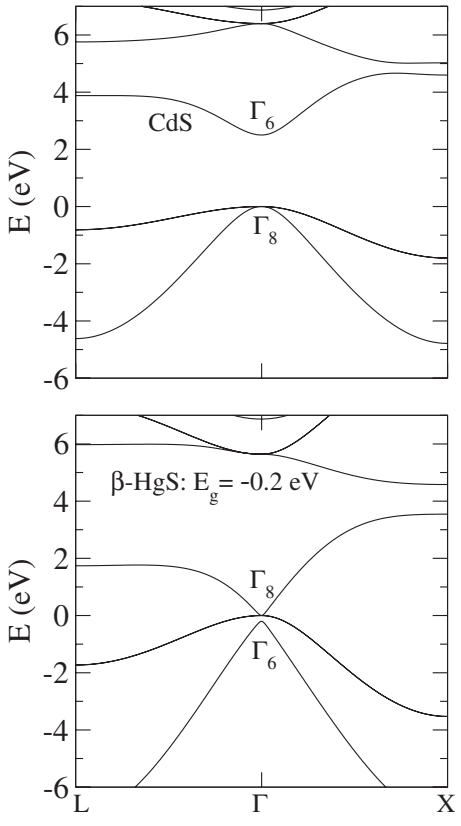


FIG. 1. Bulk band structure of CdS (upper panel) and $\beta$-HgS (lower panel). CdS has a normal band structure, with the $s$-type $\Gamma_6$ band lying above the $p$-type $\Gamma_8$ band. $\beta$-HgS has an inverted band structure where the $\Gamma_6$ band lies below $\Gamma_8$ band.

 

verted band structure where the $\Gamma_6$ band lies below the $\Gamma_8$ band, as shown in the lower panel of Fig. 1. The effective masses of the conduction and light-hole bands are negative near $\Gamma$. As a result, the two $\Gamma_8$ bands degenerate at $\Gamma$, which are light-hole and heavy-hole bands, become the lowest empty (conduction) band and highest occupied (valence) band, respectively. $\beta$-HgS, HgSe, and HgTe are classified as gapless semiconductors or semimetals with the negative gap between $\Gamma_6$ and $\Gamma_8$ bands. Due to the band inversion and the narrow-gap, conduction and valence bands are strongly mixed away from the zone center, and effective masses become momentum dependent resulting in highly nonparabolic dispersion. Experimentally, it was shown[12–14] that the level structure of HgTe and $\beta$-HgS QDs changes from inverted gap to positive gap with decreasing size. As a consequence of the strong mixing, it becomes difficult to follow levels as the QDs change from inverted gap to positive gap with decreasing size. For example, the inverted conduction band $\Gamma_6$ has a negative mass. It cannot evolve directly to a confined state above the gap in the same way that conduction states evolve due to confinement of positive-gap semiconductors with positive effective masses. Moreover, as we will show, unique intrinsic surface states strongly affect the evolution of the level structure of inverted-gap QDs. These states are not confined bulk states because they are localized toward the QD surface in large dots. However, they evolve into above-gap confined states as the dot size decreases. These surface states are not caused by dangling bonds so that they cannot be removed by surface passivation. Similar surface states have been predicted theoretically to exist on the surface of bulk negative-band-gap semiconductors[15,16] and nanocrystals.[17] The interplay of strong mixing, the inverted band structure with negative effective masses, and the contribution from intrinsic surface states will define the size evolution of QD levels and determine the optics and excitonic response of negative-gap QDs.

These properties of negative-gap nanocrystals are related to analogous effects in HgCdTe alloys and HgTe/CdTe quantum wells and superlattices investigated in the 1980s.[18,19] Indeed, by tuning the composition of an alloy such as $Hg_{1-x}Cd_xTe$, the alloy changes from a semimetal with an inverted band structure to a semiconductor with a positive gap.[18] Bastard[19] also showed that the band structure of HgTe/CdTe superlattices and quantum wells behave with decreasing width of the HgTe wells in the same way as $Hg_{1-x}Cd_xTe$ alloys for increasing $x$. It was also shown that such superlattices and quantum wells support interface states appearing between HgTe and CdTe layers.[20–22] These interface states appear only if the positive gap of the CdTe barrier overlaps the negative gap of the HgTe well.[21,23,24] The existence of the surface states has been confirmed experimentally in tunneling studies of HgCdTe surface quantum wells.[25]

Recently, the problem of surface (edge) states in negative-gap nanostructures has stimulated intense renewed interest. It was proposed that the spectrum of surface (edge) states in these structures may become gapless, and that such materials may manifest a topological insulator phase,[26–29] with important implications for quantum computing and spintronics. This possibility further motivates the need to understand the evolution of states and the influence of intrinsic surface states in negative-gap QDs.

Theoretical models used previously for the analysis of the band-structure effects in negative-band-gap nanocrystals were based on either the $\mathbf{k}\cdot\mathbf{p}$ Luttinger model[15–17] or on a simplified four-band tight-binding model.[26,29] However, a four-band model completely ignores the presence of the heavy-hole band. In negative-band-gap semiconductors, the heavy-hole valence band is degenerate with the first band above the gap at point $\Gamma$ (see Fig. 1), and it can couple both with the surface states and the inverted $\Gamma_6$ band. The Luttinger model[30] takes into account the band mixing but this model is invalid away from the zone center. Because of this, the Luttinger model cannot be used for small nanocrystals with confined states that are defined by the bulk bands away from the zone center.[31] Moreover the Luttinger model cannot account for the precise geometry of the nanocrystal and surface effects. Therefore, both the four-band tight-binding model and the Luttinger model provide an incomplete description for negative-band-gap nanocrystals.

In this paper, we study the electronic and optical properties of negative-gap QDs using a realistic atomistic tight-binding approach for the electronic-structure calculations. Previously, we successfully applied an atomistic tight-binding approach to investigate other narrow-gap nanostructures including CdS/HgS/CdS quantum-dot quantum wells.[31] Here, we study spherical $\beta$-HgS QDs with radius $2a < R < 22a$, where $a$ is the lattice constant of $\beta$-HgS. We investigate how the QD electronic structure changes with dot radius. Our results demonstrate the inversion of the QD level structure with increasing radius and the evolution of an intrinsic surface state lying in the negative gap into the lowest confined conduction state above the gap with decreasing size. We analyze the excitonic states and study how the surface state affects the optical response of the $\beta$-HgS QDs. Excitonic states are calculated using a configuration-interaction approach[32] developed for nanostructures in the strong confinement regime. We follow the scheme of Refs. 33–35 to apply this approach for the tight-binding approximation. We evaluate the excitonic binding as a function of dot size to understand the interplay of electron-hole interaction, screening, and confinement and to address the possibility of an excitonic insulator phase when the gap closes. This interplay is manifested differently in negative-gap QDs than in normal QDs made from positive-gap semiconductors. The main insight obtained for HgS in this work is general for other QDs made of negative-gap materials.

The paper is organized as follows. In Sec. II, we describe the tight-binding model and present the results for the level structure calculations of $\beta$-HgS QDs. We demonstrate the appearance of surface states and discuss their origin. In Sec. III, we give details of the exciton calculations and discuss how Coulomb and exchange effects change with QD size, using the results to address the possibility of a QD excitonic insulator phase. In Sec. IV, we discuss the optical response of QDs. A summary of the results is given in Sec. V.

## II. ELECTRONIC-STRUCTURE CALCULATIONS

We use the empirical tight-binding method to calculate single-particle (SP) energies and wave functions. Here we

briefly describe the method used and refer to Ref. 31 for details. We study spherical QDs. For $\beta$-HgS, the atoms occupy the sites of a zinc-blende lattice. Each atom is described by its valence $s$ orbital, three $p$ orbitals and a fictitious excited $s^*$ orbital included to mimic the effects of higher-lying states. Empirical on-site and nearest-neighbor coupling integrals are listed in Ref. 31. Spin-orbital coupling is not well known for HgS, so we do not consider it here. Reference 31 has a detailed discussion of spin-orbit effects. The parameters were adjusted to reproduce known band gaps and masses of bulk $\beta$-HgS. In particular, we obtain an inverted bulk band with $E_g^b=-0.2$ eV, consistent with recent experiments.[8] We ignore any possible relaxation at the QD surface. We explicitly exclude the effects of QD surface states localized on the dangling bonds by passivating the dangling bonds to push their energies far from the confined levels near the gap.[31] For partially passivated dots, any dangling-bond surface trap states near the gap strongly influence the intrinsic surface state studied here and it becomes difficult to identify the intrinsic surface state among the dangling bond states. In the calculations presented here, we passivate the dangling bonds by shifting the energy of each dangling bond by $V_s=100$ eV.[36,37] Once the QD structure is defined and the tight-binding Hamiltonian is built, we find the electron and hole energies and their wave functions by diagonalizing the Hamiltonian using an iterative eigenvalue solver.

The size dependence of the near-gap states in $\beta$-HgS QDs is shown in Fig. 2. Calculated electron energy levels are shown by unfilled (red) and filled (blue) circles and hole levels by black circles. The connecting lines indicate the evolution of levels. The dotted lines show the bulk valence ($\Gamma_8$) and inverted conduction ($\Gamma_6$) band edges. The two lower panels show the probability density on the anion plane $z=0.5a$ and on the cation plane $z=0.25a$ for the states marked in the upper panel. The plane $z=0$ passes through the QD center. In small QDs, the lowest conduction state, $S_c$, is derived mostly from cation $s$-type states. The first excited electron state $P_c$ is made primarily from cation $s$ orbitals with a smaller but significant contribution for cation and anion $p$ orbitals. The highest hole states, $P_a$, are derived primarily from the anion $p$-type states and are the heavy-hole states. $S_c$ is more localized toward the surface of the QD as shown in the lower panels [(a)–(c)] of Fig. 2. This is in contrast with the confined hole $P_a$ and electron $P_c$ states presented in the lower panels (d) and (e) of Fig. 2. It is worth noting that the maximum intensity of the (a), (b), and (c) images of the $S_c$ state is one order of magnitude higher on the cation plane than on the anion plane. This confirms the cation origin of this state. In contrast, for the anion-derived $P_a$ state, the maximum probability is larger on the anion plane than on the cation plane of image (d). With increasing size, $P_a$ shifts closer to the gap but remains primarily a heavy-hole state with little change in orbital character. $P_c$ also shifts toward the gap. However, $P_c$ becomes more light-holelike as the QD size increases, with significant increase in anion $p$-orbital content and substantial decrease in cation $s$ and $p$ orbital content. The lowest electron state $S_c$ shifts down in energy and becomes more strongly localized toward the surface. Finally at $R\approx 13a$, the state crosses the valence band edge and moves inside the valence band for $R>13a$. As size increases, the anion $p$ content increases while the cation $p$ content decreases, indicating the increased light-hole character of the state. In Fig. 2, we mark the state $S_c$ by filled (blue) circles connected by the blue lines to follow the change in $S_c$ with size. For $R>13a$, the spectrum of the QDs approaches the bulk band arrangement with a gapless spectrum. In practice, it is hard to identify which states form the conduction- and valence-band edges of the gapless spectrum without knowing the dispersion of the bands. To check the dispersion for the bulk limit, we have done calculations for the projected band structure of a HgS slab. We conclude that the conduction- and valence-band edges of the gapless spectrum are both derived significantly from the anion $p$ states ($P_a$). While the $P_c$ state forms the first excited electron state. Figure 2 shows directly the evolution of the HgS QD spectrum from direct gap to inverted gap with increasing size. It also reveals the increased localization toward the surface of $S_c$.

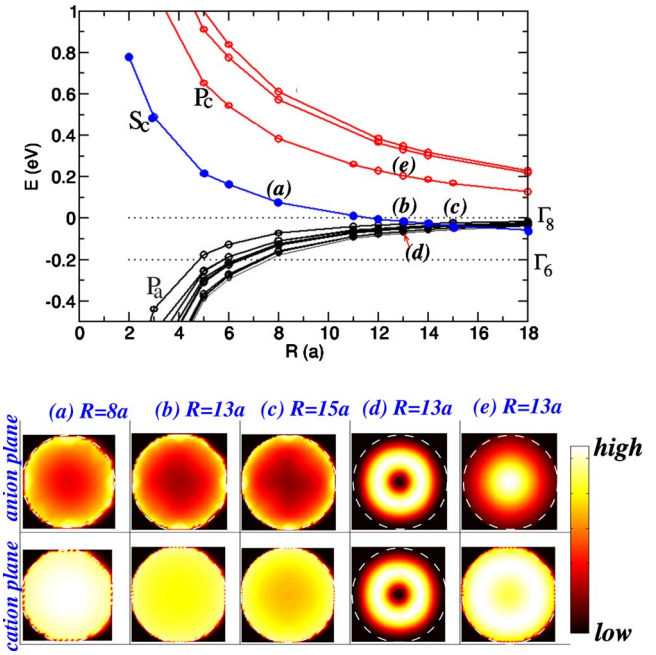


FIG. 2. (Color online) Energy levels of $\beta$-HgS QDs. The upper panel demonstrates the evolution of the near band edge levels of the QDs with radius. The electron energy levels are shown in unfilled (red) and filled (blue) and hole levels in black. The surface state is marked by the filled (blue) circles. The solid lines are guides for the eyes. The dotted lines show the bulk $\Gamma_8$ and $\Gamma_6$ band edges. The lower panels show the probability density on anion ($z=0.5a$) and cation ($z=0.25a$) planes for the states marked in the upper panel. The dashed circles outline the QD. Images (a)-(c) demonstrate the evolution of the surface state $S_c$ with increasing size. Typical confined hole $P_a$ and electron $P_c$ states are shown in (d) and (e), respectively. The maximum probability of (a), (b), and (c) is one order of magnitude higher in the cation plane than in the anion plane. The opposite is true for (d). The maximum probability in (e) is almost identical in the cation and anion planes.

It is interesting to compare the states of $\beta$-HgS with negative gap as presented in Fig. 2, with the states of QDs made of an artificial $\beta$-HgS with positive-bulk band gap $E_g^b=0.2$ eV (see Fig. 3). The levels of HgS/CdS QD quantum

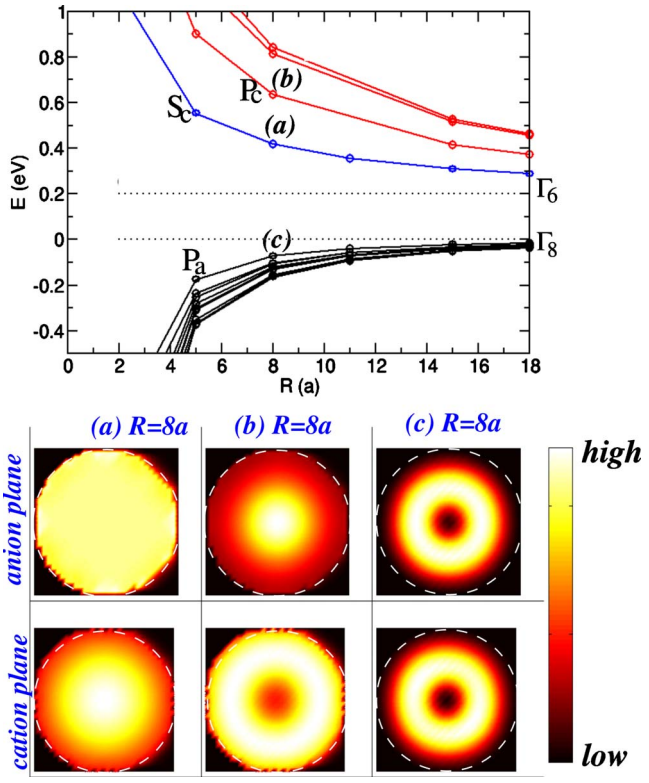


FIG. 3. (Color online) Energy levels of artificial $\beta$-HgS QDs with positive-bulk band gap $E_g^b$=0.2 eV. The upper panel demonstrates the evolution of near band-edge levels with radius, electron levels in red and blue and hole levels in black. The solid lines are guides for the eyes. The dotted lines show the bulk valence ($\Gamma_8$) and conduction ($\Gamma_6$) band edges. The two lower panels show the probability density on anion ($z$=0.5$a$) and cation ($z$=0.25$a$) planes for the states marked in the upper panel. The dashed circles outline the QDs. The maximum probability of (a) is one order of magnitude higher in the cation plane than in the anion plane. The opposite is true for (c). The maximum probability of (b) is similar in the cation and anion planes.

wells with both positive and negative-bulk band gaps have been discussed in detail in Ref. 31. Confinement acts normally on the band-edge levels of QDs with positive-bulk gap resulting in a continuous increase in levels and gaps with decreasing size. Importantly, all near band edge states are confined inside the dots without any localization toward the surface as shown in the lower panel (a), (b), and (c) of Fig. 3. All QD states converge to bulk states with increasing size when the bulk gap is positive.

The inverted-gap QDs support a surface state while the positive-gap QDs do not. This surface state is intrinsic, not caused by dangling bonds, because all dangling bonds are pushed far from the gap by passivation. For small passivating potentials ($|V_s|<10$ eV), the surface state and the energy levels of small QDs are sensitive to the magnitude of the potential.[36,37] This sensitivity to surface potential makes these QDs very attractive for applications as infrared nanosensors.

To understand the origin of the surface state, we follow the states as $R$ increases, approaching the bulk limit. The highest hole states $P_a$ and the first excited electron states $P_c$ are similar in negative-gap and positive-gap QDs as shown in the lower panels of Figs. 2(d) and 2(e) and Figs. 3(b) and 3(c). With increasing QD size, $P_a$ ($P_c$) evolves to the bulk valence $\Gamma_8$ band edge (a bulk conduction band above the gap) both for negative-gap and positive-gap QDs. $S_c$ is inherently different in the negative- and positive-gap QDs. In positive gap $\beta$-HgS, $S_c$ evolves to an above-gap bulk state $\Gamma_6$ as $R$ increases. In negative gap $\beta$-HgS, $S_c$ evolves to a level *inside* the inverted band gap, between $\Gamma_6$ and $\Gamma_8$ bulk band edges, that has no counterpart in the bulk. $S_c$ never reaches the $\Gamma_6$ band edge for negative-gap dots. In practice, we cannot model large enough dots to reach completely the "bulk" limit. To check the behavior for the bulk limit, we have done calculations for the states confined in a HgS slab. We conclude that the confined $S_c$ level evolves from a surface state *intrinsic* to the negative-gap QDs studied. Thus, $S_c$ is not a confined bulk state. The confined bulk $\Gamma_6$ levels in negative gap dots and slabs are actually pushed to more negative energies, further away from the gap. As the dot size increases for $R>13a$ and $S_c$ is pushed down into the negative gap, $S_c$ crosses the higher-lying valence states and is strongly hybridized with them. This hybridization has important consequences for the level structure, which becomes clearer for slab states with finite wave vector. For example, in a QD, the highest-lying $P_a$ state is heavy-holelike. In wide slabs, the band-edge, zone-center (in-plane wave vector $k$=0) $P_a$ valence state remains heavy-holelike after it has crossed with $S_c$. However, for finite $k$, the highest valence state in a slab becomes light-holelike with negative effective hole mass, lying above the other heavy-hole bands, just as in the bulk. This complex evolution of the dispersion of valence states in slabs of negative-gap materials and the connection to topological insulator phases will be discussed in another paper.

The size evolution of the spectrum of $\beta$-HgS QDs and appearance of the surface state demonstrated in Fig. 2 are very similar to that for CdTe/HgTe/CdTe quantum wells reported in Ref. 21. For CdTe/HgTe/CdTe quantum wells, the localized states are trapped at the interface between the negative-gap HgTe and the positive-gap CdTe. Such interface states appear if the positive gap of the CdTe barrier overlaps in energy with the negative gap of the HgTe well.[20,21,24] For $\beta$-HgS QDs with a surface, the vacuum (with infinite band gap) plays the same role as the positive-gap CdTe barrier.

## III. EXCITON STATES

To identify the effects of the inverted gap—positive-gap crossover and the intrinsic surface states on the optics of $\beta$-HgS QDs, we analyze the electron-hole correlation effects that determine exciton states. We employ a configuration-interaction approach using the tight-binding approximation for the single-particle states.[33–35] The exciton wave function is expanded in terms of the electron-hole pair states found from the tight-binding calculations

$$\Psi_{ex} = \sum_{e=1}^{N_e} \sum_{h=1}^{N_h} C_{eh} \psi_e \psi_h, \tag{1}$$

where $N_e$ and $N_h$ are the number of electron and hole states, with wave functions $\psi_e$ and $\psi_h$, included in the configuration.

The $|C_{eh}|^2$ define the occupation numbers of the electron-hole pairs. The exciton spectrum is found from the Schrodinger equation $H\Psi_{ex}=E\Psi_{ex}$. The matrix elements of the electron-hole Hamiltonian $H$ are calculated as[35]

$$H_{eh,e'h'} = (E_e - E_h)\delta_{e,e'}\delta_{h,h'} - J_{eh,e'h'} + K_{eh,e'h'}. \quad (2)$$

Here the difference between electron and hole energies, found from tight-binding calculations, defines the single-particle band gap $E_{eh}^{sp}=E_e-E_h$. The matrix elements $J$ and $K$ describe the Coulomb and exchange interactions, respectively. To obtain excitonic levels, we diagonalize the configuration-interaction matrix Eq. (2). We include a sufficient number of electron $N_e$ and hole $N_h$ states in the configurations to achieve convergence of the first few exciton states within a few millielectron volt. For the HgS QDs studied, we used the three or four lowest electronic states and the nine or ten highest hole states to ensure the convergence of the exciton states. Since we neglect the spin-orbit interaction, exciton states must be singlet (with total spin equal to 0) or triplet (with total spin equal to 1).[38] The exchange matrix elements vanish for triplet states. Therefore, there are two Hamiltonians depending on the exciton spin. The Hamiltonian for singlet exciton (SE) states includes both the Coulomb and exchange interactions while the Hamiltonian for the triplet exciton states includes only the Coulomb interaction. We diagonalize these two Hamiltonians separately to obtain the spectra of the singlet $E_n^{ex,s}$ and triplet $E_n^{ex,t}$ excitons.

The Coulomb and exchange interactions are screened by a dielectric function $\epsilon(|\vec{r}'-\vec{r}|,R)$ which depends both on spatial separation between electrons and holes $|\vec{r}'-\vec{r}|$, and the QD radius $R$. The size dependence of the dielectric function explicitly defines the extent of screening and the dielectric confinement effect.[39] Calculations of the average dielectric constant in nanostructures show that it decreases with size.[40,41] However, the origin of this decrease is not understood.[42] In the Thomas-Fermi approach,[40] the decrease in the dielectric constant is attributed to the decrease in the polarizability due to increasing gap. On the other hand, it was proposed[42] that the decrease in the average dielectric response with decreasing size could be caused by the breaking of polarizable bonds at the surface. In this case, the dielectric screening can be described by the bulk size-independent dielectric function except the thin surface layer of the order of the Fermi wavelength.

Following the approach of Ref. 43, we approximate the electronic (high-frequency) dielectric function by the Thomas-Fermi model,[44] and the ionic (low-frequency) dielectric function by the polaronic model.[38] The electronic dielectric function of the dot is obtained from a Penn model[43]

$$\epsilon_\infty^{dot} = 1 + (\epsilon_\infty^{bulk} - 1)\frac{[E_g^b + \Delta E]^2}{[E_g^d(R) + \Delta E]^2}. \quad (3)$$

Here $E_g^d(R)$ is the calculated band gap of the QD, $\epsilon_\infty^{bulk}$ is the bulk high-frequency dielectric constant equal to 11.36 for $\beta$-HgS, and $E_g^b+\Delta E$ is the energy of the first pronounced peak in the bulk absorption spectrum. In accordance with experimental data,[10] we assumed that $E_g^b+\Delta E$ is equal to 0.25 eV both for the inverted band $\beta$-HgS with $E_g^b=0$ and for the artificial direct band $\beta$-HgS with $E_g^b=0.2$ eV. The low-frequency dielectric constant of the dot is obtained as

$$\epsilon_o^{dot}(R) = \epsilon_\infty^{dot} + (\epsilon_o^{bulk} - \epsilon_\infty^{bulk}), \quad (4)$$

where $\epsilon_o^{bulk}$ is the bulk low-frequency dielectric constant, equal to 18.2 for $\beta$-HgS. We perform the calculations using size-dependent dielectric function as defined by Eqs. (3) and (4). We also perform calculations with the bulk size-independent dielectric function. This allows us to test the robustness of our predictions to different choices for screening.

We use the two-orbital approximation[34] to evaluate $J$ and $K$. This allows us to expand $J$ and $K$ into a small number of Coulomb-type $\omega_{coul}$ and exchangelike $\omega_{exch}$ integrals using the tight-binding wave functions $\psi_{e,h}$. To evaluate screened and unscreened on-site integrals $\omega_{coul}$ and $\omega_{exch}$, we used a reciprocal-space formalism.[33,43] Off-site integrals $\omega_{coul}$ and $\omega_{exch}$ between nearest neighbors were calculated by direct integration in real space. All other off-site Coulomb integrals were estimated using the Ohno formula[45] modified to include screening.[34] Working with the empirical tight-binding approach, we must choose atomic basis functions for the evaluation of the $\omega_{coul}$ and $\omega_{exch}$ integrals. There are several choices for the basis functions. These include the Slater-Koster orbitals,[46] which have an analytical formulation; and Hermann-Skillman orbitals[47] which can be obtained by numerical atomic-structure calculations. The Slater-Koster orbitals allow us to get analytical matrix elements. However, the Hermann-Skillman orbitals should correspond more closely to the actual atomic states. We used both the Slater-Koster orbitals and Hermann and Skillman orbitals to evaluate $\omega_{coul}$ and $\omega_{exch}$. Although the values of the integrals may differ considerably for the two choices of the orbitals, the trends for the excitonic effects are qualitatively identical. In all results presented here, we use the Coulomb and exchange integrals calculated using Hermann-Skillman orbitals.

The configuration-interaction matrix (2) is defined by the transitions from the filled to the empty electron levels, which are separated by the Fermi level. In principle, the Fermi level can be determined by finding all electron levels and filling them with the atomic valence electrons. This computational approach is not practical for large dots. Even so, for a dot with a positive gap, strict filling of just the valence states, leaving the conduction states empty, is achieved only for dots with an equal number of anions and cations. Surface passivation should account for any charge imbalance on the dot. To account for this effect of the surface passivation, we would need an explicit, atomistic model for the passivants. This is beyond the scope of our model. Instead, we follow the routinely used practice of taking the Fermi level between the valence and conduction bands, as in the bulk. This choice for the Fermi level is clear for small HgS dots with a finite, positive gap, but not clear if the gap closes and conduction levels move into the valence band. The level schemes we use are shown in Fig. 4. We indicate in Fig. 4 the single-particle energy levels used in the configuration-interaction matrix in Eq. (2). The line thickness of each level indicates the level degeneracy. The allowed transitions that correspond to ab-

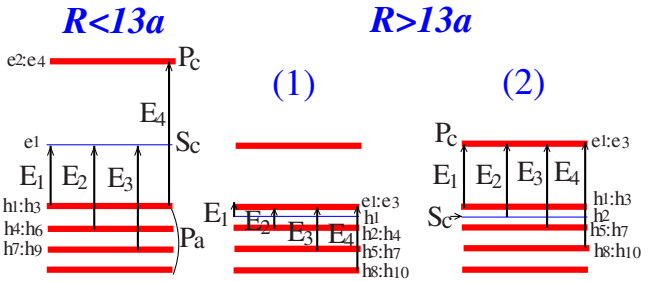


FIG. 4. (Color online) Schematics of the single-particle energy levels taken into account for the excitonic calculations. The line thickness of each level indicates the level degeneracy. The arrows show the allowed transitions $E_1$, $E_2$, $E_3$, and $E_4$ ordered in energy.

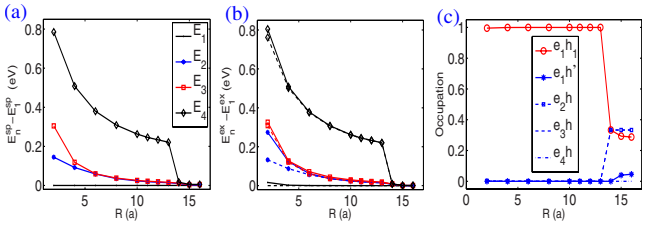


FIG. 5. (Color online) Splitting of the (a) four lowest single-particle transition energies $E_n^{sp}-E_1^{sp}$ and (b) four lowest exciton levels $E_n^{ex}-E_1^{ex}$. The singlet and triplet states are shown by the solid and dashed curves, respectively. Occupation of the lowest singlet exciton state (c). Filling scheme 1 was used for this calculations for $R>13a$.

sorption are shown by arrows. For small QDs ($R<13a$) the band gap between the lowest cation-derived $s$-type electron state $S_c$ and the highest $p$-type hole state $P_a$ is clear [see Fig. 4]. However, for $R>13a$ the band gap becomes ambiguous because the $S_c$ moves into the valence band. Results should depend on which valence states and whether $S_c$ are occupied in the ground state. We consider the two possible filling configurations for $R>13a$, shown in Fig. 4. In filling scheme 1, the lowest empty state was chosen to be the highest anion-derived $p$-type state $P_a$. In scheme 2, we assume that $P_c$ is the lowest unoccupied state. Given the uncertainty in the level filling because of the nonstoichiometry of the dot and the unknown amount of charge accounted for by the passivation, we test both filling schemes.

The filling schemes we consider are "closed shell" schemes with the highest occupied molecular orbital (HOMO) completely filled and the lowest unoccupied molecular orbital completely empty in the nanocrystal ground state. This closed shell scheme is commonly used and works well to describe QDs with a wide gap. However, as mentioned above, the filling scheme to be used is not obvious when the gap is small or negative. We consistently use the closed shell scheme even for $R>13a$. After $S_c$ crosses $P_a$, two closed shell schemes are possible. We consider both. However, one could also assume that when $S_c$ crosses below $P_a$ and captures two electrons, $P_a$ loses two electrons and becomes partially occupied. This is an "open shell" filling scheme. Correlation effects between electrons in the partially occupied $P_a$ HOMO would have to be included to determine the nanocrystal ground state for a partially occupied HOMO. This scheme should also be considered but is beyond the scope of the calculations presented here.

When the gap is small or negative (i.e., for $R$ near $13a$), electron-hole binding energy can be comparable to the gap as well. In that case, correlation and binding energy from electron-hole excitations should also be included to determine the nanocrystal ground state. Such an excitonic insulator ground state should also be considered but is beyond the scope of the calculations discussed here.

In Fig. 5, we compare the splitting of four lowest exciton levels $E_n^{ex}-E_1^{ex}$ (b) with the single-particle transition-energy splittings $E_n^{sp}-E_1^{sp}$ (a). Both the singlet (solid curves) and triplet (dashed curves) states are shown. We define the occupation numbers $C_{e_ih}=\Sigma_j|C_{e_ih_j}|^2$, where the sum is over all hole states included in the configuration. In Fig. 5(c), we show the $C_{e_ih}$ of the lowest singlet exciton state as a function of the QD radius. Here we separated the occupation number $|C_{e_1h_1}|^2$ (circles) corresponding to $E_1$ transition in Fig. 4. The curve with stars corresponds to $C_{e_1h'}=C_{e_1h}-C_{e_1h_1}$. The occupation numbers of the next two exciton levels are similar to that of the lowest state shown in Fig. 5(c) but the label $e_1h_1$ must be replaced for $e_1h_n$ with $n=2,3$ for the second and third states, respectively. For $R>13a$, scheme 1 was used for these calculations. The kink for the fourth exciton level and the fourth single-particle transition energy arises from the change in the filling used for $R<13a$ to the filling used for $R>13a$ shown in Fig. 4.

An important feature of the results shown in Fig. 5(a) is that the single-particle splittings cannot be fit by the $1/R^2$ function that is characteristic of normal (particle in a box) confinement. Instead, $E_n^{sp}-E_1^{sp}$ scale as $1/R^\alpha$ where $\alpha=0.8$, 1, and 0.7 for $n=2,3,4$, respectively, decaying much slower with increasing $R$ than is typical for quantum confinement. The triplet exciton splittings follow closely the single-particle transition energy splittings. The singlet exciton states are split from the triplet states by the exchange interaction. Due to quantum confinement enhancement of the electron-hole spatial overlap,[48–50] the exchange splittings for all four levels increase with decreasing QD size. As shown in Fig. 5(b), the exchange splitting for the second exciton level is larger than for the other levels. For small QDs, the second exciton state is mostly defined by the electron-hole pair composed of the $S_c$ electron state and the second $P_a$ hole state [see transition $E_2$ in Fig. 4]. For large QDs, all $P_a$ hole states included in the configuration are composed mostly of anion $p$ orbitals. However, with decreasing size, the second $P_a$ hole level gains considerable contribution from $s$-cation orbitals. This feature is a consequence of the band mixing in the strong confinement regime. In contrast, the other hole states remain mostly anion derived $p$ states with decreasing size. The coupling between the cation $s$ orbitals of $S_c$ and the second $P_a$ level results in much larger exchange splitting of the second exciton level than the coupling between the cation $s$ orbitals $S_c$ and the anion $p$ orbitals of the hole states of the other exciton levels shown in Fig. 5(b).

The occupation numbers change abruptly for $R>13a$ as shown in Fig. 5(c). Such behavior is characteristic of the three lowest exciton states both of singlet and triplet-type. For $R<13a$, the lowest exciton state is composed mostly of

the $e_1h_1$ electron-hole pair. The mixing of electron-hole pairs does not increase with increasing size. This result is counterintuitive. For normal (particle-in-the-box) confinement, mixing is enhanced with increasing size because the corrections to the wave function caused by the mixing scales in lowest-order perturbation theory, as

$$\frac{J_{n1}}{E_n^{sp} - E_1^{sp}} \sim \frac{\frac{1}{R}}{\frac{1}{R^2}} \sim R. \tag{5}$$

Here $J_{n1}$ is the Coulomb matrix element between $n$th and first electron-hole pairs which scales approximately as $1/R$. However, as discussed above for negative-gap QDs, $E_n^{sp} - E_1^{sp} \sim 1/R^{\alpha}$ where $\alpha=0.8$, 1, and 0.7 for $n=2,3,4$, respectively. As a result, the mixing even decreases with size as $R^{\alpha-1}$ for the lowest exciton states and the exciton states become more like noninteracting pair states as $R$ increases up to the gap closure. As the gap closes, screening is enhanced [see Eq. (3)], becoming more metallic. This also suppresses mixing. However, even when we use size-independent screening, mixing does not increase with increasing size. The dominant effect is the slow decrease in the energy gaps and levels with increasing size. For $R>13a$ after the collapse of band gap, all electron-hole pairs strongly mixed in the configuration. The nonmonotonic behavior of $C_{e_ih_j}$ is a signature for the transition between positive and inverted gaps.

The lowest singlet exciton state, $E_1^{ex,s}$, defines the optical gap $E_g^{ex}=E_1^{ex,s}$. The exciton binding energy (Coulomb splitting) is the difference between the single-particle band gap, $E_g=E_1^{sp}$, and the lowest triplet state, $\Delta E_{coul}=E_g-E_1^{ex,t}$. The exchange splitting is the difference between the lowest singlet and triplet states, $\Delta E_{exch}=E_1^{ex,s}-E_1^{ex,t}$. In Fig. 6(a), we compare $E_g^{ex}$ (circles) with the single-particle band gap $E_g$ (squares) and the difference between $S_c$ and the highest $P_a$ level, $E_{Sc}-E_{Pa}$ (thin curve). Figures 6(b) and 6(c) show the Coulomb and exchange splittings, respectively. In the right panels of Figs. 6(a)–6(c)), we zoom in on the region close to gap closure. The solid and dashed curves in Figs. 6(a)–6(c) are found with filling schemes 1 and 2, respectively. To distinguish how dielectric screening and quantum confinement affect the Coulomb and exchange energies, we also show $E_g^{ex}$, $\Delta E_{coul}$, and $\Delta E_{exch}$ calculated with the size-independent dielectric function corresponding to the bulk dielectric constants (dashed-dotted curves). On the large scale, both the exciton and single-particle ground-state energies, as well as the exchange splitting, decrease monotonically with radius for scheme 1, as shown in the left panel of Fig. 6. In contrast, for filling scheme 2 the energy of the exciton ground state and the exchange splitting jump for $R>11a$ as shown by the dashed curves in the left panels of Figs. 6(a) and 6(c). However when we zoom on the region close to gap closure, we notice that no quantities behave monotonically for any scheme used. As we show below, this nonmonotonic behavior is related to the positive-inverted gap crossover and surface states.

For $R<12a$, $E_{Sc}-E_{Pa}$ [the thin curve in Fig. 6(a)] defines the single-particle gap $E_g$ of the dot. For $R>13a$, $E_{Sc}-E_{Pa}$ becomes negative, indicating the transition from positive-gap to inverted-gap and $E_g$ depends on the filling scheme. In this region, the energy of the exciton ground state becomes negative [see squares in the right panel of Fig. 6(a)], with the exciton binding energy, $E_b^{ex}=\Delta E_{coul}$, larger than the lowest single-particle gap, $E_g$. This indicates that the normal insulating ground state with filled valence band becomes unstable against the formation of electron-hole pairs, and defines the size for a transition to a possible excitonic insulator phase.[3] Importantly, $E_g^{ex}$ calculated with a size-independent dielectric function also becomes negative for $R>13a$ [see dashed-dotted curve in the right panel of Fig. 6(a)]. This implies that a prediction of an excitonic insulator phase does not depend on the model of the dielectric screening used. In filling scheme 2, the energy of the exciton ground state shows a kink for $R>11a$ but remains positive [see the dashed curve with squares in the left panel of Fig. 6(a)]. The excitonic insulator phase in the $\beta$-HgS QDs is possible but it will depend on the filling of the valence states or on the level of doping.

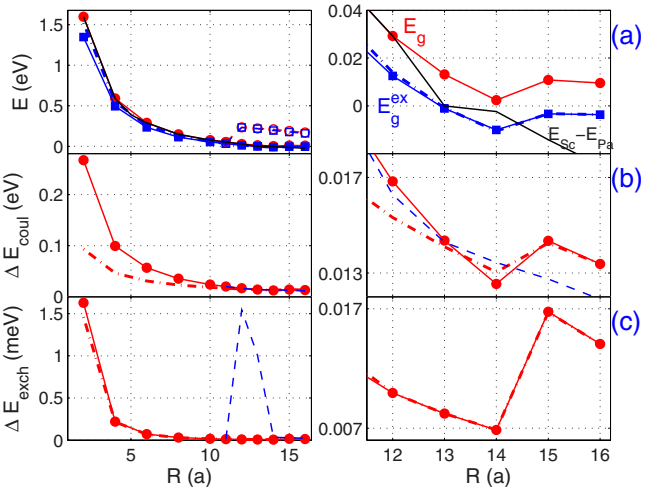


FIG. 6. (Color online) Size dependence of (a) the single-particle band gap $E_g$ (circles), the exciton ground state $E_g^{ex}$ (squares), and $E_{Sc}-E_{Pa}$ (thin curve); (b) the Coulomb splitting $\Delta E_{coul}$; (c) the exchange splitting $\Delta E_{exch}$; right panels zoom in on the size region close to gap closure. The solid and dashed curves are for filling schemes 1 and 2, respectively. Dash-dotted curves in (a), (b), and (c) show $E_g^{ex}$, $\Delta E_{coul}$, and $\Delta E_{exch}$ calculated with a size-independent dielectric function corresponding to the bulk dielectric constant.

As seen in Fig. 6(a), the energy of the exciton ground state follows closely the single-particle band gap for either filling scheme. For $R<10a$, both $E_g$ and $E_g^{ex}$ can be roughly fit by a $1/R^{1.5}$ function which differs from $1/R^2$ characteristic of normal (particle-in-the-box) confinement. The binding energy and exchange splitting rapidly decrease in the interval $2a<R<10a$ [see left panels of Figs. 6(b) and 6(c)]. $\Delta E_{coul}$ roughly scales as $1/R^{1.5}$, which is steeper than the $1/R$ scaling expected for a Coulomb energy with size-independent screening [see dashed-dotted curve in the left panel of Fig. 6(b)]. This is a signature of the increased screening near gap closure. On the other hand, the exchange energy is almost insensitive to screening. In Fig. 6(c), the solid and dashed-dotted curves can be distinguished for $R<4a$ only. Our re-

sults demonstrate that for small QDs $\Delta E_{exch}$ scales as $1/R^3$. This agrees with enhancement of the electron-hole exchange interaction in QDs predicted in Ref. 51.

The solid and dashed curves for $\Delta E_{coul}$, corresponding to filling schemes 1 and 2, almost coincide in Fig. 6(b). In contrast, the exchange splitting is more sensitive to the level filling. Our results demonstrate a sharp peak in the exchange splitting at $R \approx 13a$ for filling scheme 2 [see dashed curve in the left panel of Fig. 6(c)]. Coulomb-interaction couples the electron $|\psi_e|^2$ and hole $|\psi_h|^2$ charge densities. The charge densities of the relevant states are similar for both filling schemes. As a result on the large scale, $\Delta E_{coul}$ is only weakly dependent on the filling scheme used. The exchange interaction is defined by the Coulomb coupling between polarization densities $\psi_e \psi_h$. For scheme 2, the polarization density is a maximum for $R \approx 13a$, when both $\psi_e$ and $\psi_h$ are defined by cation derived states ($P_c$ and $S_c$) [see transition $E_2$ in the right panel of Fig. 4]. This is in contrast with all other cases when $\psi_e$ and $\psi_h$ are defined by the cation-derived ($S_c$ or $P_c$) and anion-derived ($P_a$) states. For scheme 1, the exchange and Coulomb splittings are also sensitive to the positive-inverted band-gap transition on the small scale [see the right panels of Figs. 6(b) and 6(c)]. The surface-localized state $S_c$ defines the band edge for $R < 14a$ [see the thin curve in the right panel of Fig. 6(a)], so the ground exciton state is defined by the transitions between cation-derived ($S_c$) and anion-derived ($P_a$) states. For $R > 14a$ the exciton is defined by the transitions between anion derived $p$-type states. This results in the steplike increase in $\Delta E_{coul}$ and $\Delta E_{exch}$ at $R = 15a$ shown in the right panels of Figs. 6(b) and 6(c).

## IV. OPTICAL RESPONSE

To determine the single-particle and exciton optical spectra of $\beta$-HgS QDs, we calculate the optical response in the dipole approximation

$$\sigma(\hbar w) \sim \sum_{\alpha} |\vec{E} \cdot \vec{D}_{\alpha}| \delta(E_{\alpha} - \hbar w), \tag{6}$$

where the sum is over all transitions $\alpha$ and $E_{\alpha}$ is the transition energy, $\vec{E}$ is the electric field, and $\vec{D}_{\alpha}$ is the dipole moment. In the single-particle approximation, the transition energy is defined by the single-particle pair energy between $i$th electron and $j$th hole levels, $E_{\alpha} = E_{ij} = E_{ei} - E_{hj}$, and the dipole moment is $\vec{D}_{\alpha} = \vec{D}^o_{ij} = \langle \psi_{ei} | \vec{r} | \psi_{hj} \rangle$. For the exciton optical response, the transition energy is the energy of the $\alpha$th exciton level $E_{\alpha} = E^{ex}_{\alpha}$. The dipole moment is[34]

$$\vec{D}_{\alpha} = \sum_{e,h} (C^{\alpha}_{eh})^* \vec{D}^o_{eh}, \tag{7}$$

where the sum runs over all electron-hole pairs included in the exciton configuration. In the dipole approximation, spin flips are not allowed, and only the singlet exciton states can absorb light. We first calculate the single-particle dipole moments $\vec{D}^o_{ij}$ using the tight-binding wave functions as described in Ref. 31. Using the single-particle dipole moments and the coefficients $C^{\alpha}_{eh}$ of the exciton wave functions we evaluate the exciton dipole moment and calculate the exciton optical response. For all calculations we use filling scheme 1 for allowed transitions.

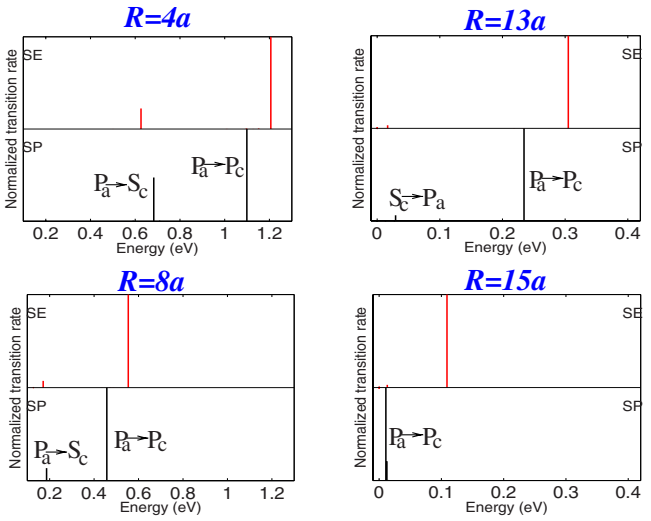


FIG. 7. (Color online) Normalized transition rates for HgS QDs with radii $R=4a$, $8a$, $13a$, and $15a$. (lower panels) SP spectra, (upper panels) bright SE spectra. Single-particle transitions are indicated.

We show in Fig. 7 how the optical response changes with radius. The transitions to the singlet exciton states are allowed, they correspond to the bright exciton spectrum. For each QD size, we show the SP and SE spectra in the lower and upper panels, respectively. For small QDs with a positive gap, $(R=4a, 8a)$ the $P_a \rightarrow S_c$ transition is the lowest bright transition. As shown in Fig. 5(c), the Coulomb and exchange interaction do not mix the electron-hole pairs, so the energy of this state is defined from the electron-hole pair roughly as $E^{ex}_n \sim E^{sp}_n - J_{nn} + K_{nn}$ [see Eq. (2)]. The Coulomb interaction is larger than exchange interaction, $J_{nn} > K_{nn}$, so the first exciton peak is redshifted from the single-particle peak shown in Fig. 7. The second absorption peak is related to the transition $P_a \rightarrow P_c$. As mentioned, the $P_c$ state has similar probability density on anion and cation planes, giving rise to a strong exchange and Coulomb interaction of the $P_c$ and $P_a$ states in the anion plane. A strong mixing of the $e_i h_j$ $(i=2:4,\ j=1:9)$ electron-hole pairs in the highest exciton states blueshifts the second exciton absorption peak from the single-particle transition as shown in Fig. 7. With increasing dot size, the strength of the $P_a \rightarrow S_c$ transition decreases relative to the $P_a \rightarrow P_c$ transition so that the $P_a \rightarrow P_c$ transition defines the dominant low-energy absorption peak for $R > 6a$.

For $R \approx 13a$, the gap collapses, the level structure is inverted and $S_c$ is localized more toward the surface. Consequently, the transition $P_a \rightarrow S_c$ is inverted to $S_c \rightarrow P_a$. For $R > 13a$ the $S_c \rightarrow P_a$ transition is weak. The higher, strongly mixed exciton states, related to the $P_a \rightarrow P_c$ transition, completely define the exciton spectra after the band-gap closure as shown in the right panel of Fig. 7.

We summarize these results in Fig. 8 by presenting the size dependence of the strongest optical transitions. The low-energy exciton absorption peak (solid curve) is redshifted from the single-particle transition $P_a \rightarrow S_c$ (dashed curve).

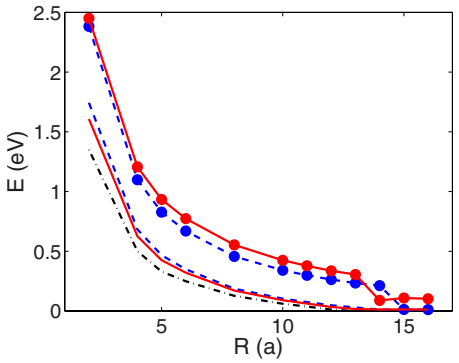


FIG. 8. (Color online) The size dependence of the strongest optical transitions of $\beta$-HgS QDs. The emission threshold defined by the energy $E_1^{ex,t}$ is shown by the dashed-dotted curve. The energies of the single-particle and corresponding singlet exciton $P_a \rightarrow S_c$ transition are shown by dashed and solid curves, respectively. The energies of the single-particle and corresponding singlet exciton $P_a \rightarrow P_c$ transition are shown by dashed and solid curves with circles, respectively.

The dominant exciton absorption peak (solid curve with circles) is blueshifted from the single-particle transition $P_a \rightarrow P_c$ (dashed curve with circles). We can see that in this scheme the emission threshold (dashed-dotted curve) changes monotonically with QD size, while a dominant absorption line shows a steplike behavior. The nonmonotonic change in the optical spectra close to the inversion is a signature for the transition from positive to inverted gap.

The $P_a \rightarrow S_c$ transition involves the state which becomes more localized toward the QD surface with increasing size, as shown in lower panels (a), (b), and (c) of Fig. 2. The $P_a \rightarrow P_c$ transition is between two confined states [see lower panels (d) and (e) in Fig. 2]. As mentioned, with increasing dot size, the strength of the $P_a \rightarrow S_c$ transition decreases relative to the strength of the $P_a \rightarrow P_c$ transition. To quantify the effect of surface state on optical response, we compare in Fig. 9 the ratio of dipole moments for the transitions $P_a \rightarrow S_c$ and $P_a \rightarrow P_c$, $D_{n(p)}=D_{n(p)}^{ps}/D_{n(p)}^{pp}$ for negative ($n$) gap and positive gap ($p$) dots. The curve with squares shows the ratio $D_p/D_n$ for the single-particle transitions, and the curve

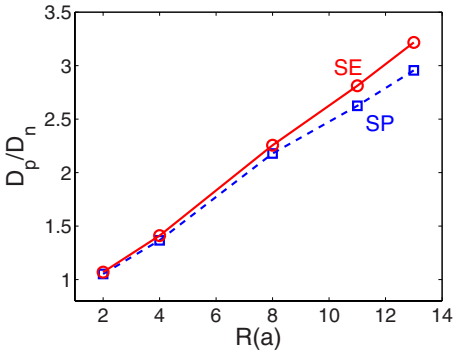


FIG. 9. (Color online) Size dependence of the ratio $D_p/D_n$ for QDs with positive- and negative-bulk band gap. The solid curve with circles shows the ratio for the exciton singlet dipole moment, and the dashed curve with squares shows the ratio for the single-particle dipole moment.

with circles shows the ratio for the corresponding exciton singlet transitions. The ratio $D_p/D_n$ increases with increasing radius both for the single-particle and exciton dipole moment, so that at $R=13a$ $D_p$ is more than three time larger than $D_n$. The behavior of $D_p/D_n$ correlates with the increased localization of $S_c$ toward the surface with increasing QD size. The relative strength of the transition $P_a \rightarrow S_c$ could be used to test the intrinsic surface state character of the $S_c$ state in $\beta$-HgS QDs.

## V. SUMMARY

Using an atomistic tight-binding approach, we have investigated the size evolution of single-particle states in QDs made from negative-bulk-band-gap semiconductors such as $\beta$-HgS. With decreasing size, the QD level structure changes from an inverted gap to a positive gap. Size tuning provides the control needed to exploit these dots as far-IR nanosensors with very small gaps. In small dots, the lowest electron level behaves like a confined level in a dot made from a positive-gap semiconductor. As the size of the HgS dot increases, the lowest conduction level crosses the gap, moving below the valence-band edge. However, it does not converge to the bulk-inverted band edge. Rather, it approaches a limit inside the inverted gap, revealing that its parent state in the bulk limit is a surface state intrinsic to the dot, not a bulk band state. The surface localization of this state makes it an ideal state to exploit for sensor applications requiring surface sensitivity. The origin of the surface state is similar that of surface states found in the HgTe quantum-well structures. Near gap closure there is also strong band mixing. As a result, the levels and gaps between levels decrease more slowly than the usual $1/R^2$ scaling. This slow scaling has important consequences for exciton states.

We have investigated the optical response and exciton states of these QDs using a configuration-interaction approach. The positive-inverted gap transition manifests itself in the nonmonotonic size dependence of the excitonic effects and optical response of the QDs. In small dots, the lowest exciton states are defined by the noninteracting electron-hole pair states with the low-energy exciton absorption peak redshifted from the single-particle transition by the Coulomb and exchange energy. As QD size increases, the level splittings remain the dominant energy scale, decreasing more slowly than the interaction energy so that the exciton remains nearly a noninteracting electron-hole pair even up to the gap closure. After the collapse of gap, all electron-hole pairs are strongly mixed by the Coulomb and exchange interactions and contribute similarly to the exciton states. As a result the dominant optical absorption of the QDs changes steplike when passing through positive-inverted gap transition. The surface state is evident in the excitonic effects and in optical spectra and is responsible for a reduction in the transitions strength near the gap closure.

Close to the gap closure the exciton binding energy becomes larger than the lowest single-particle gap, making the filled ground state unstable to the formation of electron-hole pairs and raising the possibility of an excitonic insulator phase for these nanocrystals. This possibility depends on the

level of doping in the QDs. This excitonic insulator phase is robust and does not depend on the model of the dielectric screening used. This makes negative-band-gap nanocrystals attractive for testing new QD phases.

In this paper, we neglected the spin-orbit interaction because of the uncertainty in parameters. It is important to know how the trends discussed here might be affected by spin-orbital coupling. Analysis shows that intrinsic surface states and the band-gap collapse are evident in negative gap HgTe films where the parameters of the spin-orbital coupling are known. Optical response and excitonic effects must be affected by spin-orbital coupling due to the mixing of singlet and triplet exciton states. This problem needs further investigation.

*nmalkova@nist.gov


[1] J. N. Schulman and T. C. McGill, Appl. Phys. Lett. **34**, 663 (1979).
[2] S. V. Kershaw, M. Harrison, A. L. Rogach, and A. Kornowski, IEEE J. Sel. Top. Quantum Electron. **6**, 534 (2000).
[3] D. Jérome, T. M. Rice, and W. Kohn, Phys. Rev. **158**, 462 (1967); J. Zittartz, *ibid.* **164**, 575 (1967).
[4] M. Buttiker, Science **325**, 278 (2009).
[5] K.-U. Gawlik, L. Kipp, M. Skibowski, N. Orlowski, and R. Manzke, Phys. Rev. Lett. **78**, 3165 (1997).
[6] C.-Y. Moon and S.-H. Wei, Phys. Rev. B **74**, 045205 (2006).
[7] A. Delin, Phys. Rev. B **65**, 153205 (2002).
[8] K. Dybko, W. Szuszkiewicz, E. Dynowska, W. Paszkowicz, and B. Witkowska, Physica B **256-258**, 629 (1998).
[9] A. Mycielski, J. Kossut, M. Dobrowolska, and W. Dobrowolski, J. Phys. C **15**, 3293 (1982).
[10] R. Zallen and M. Slade, Solid State Commun. **8**, 1291 (1970).
[11] M. von Truchseß, A. Pfeuffer-Jeschke, C. R. Becker, G. Landwehr, and E. Batke, Phys. Rev. B **61**, 1666 (2000).
[12] B. K. Patel, S. Rath, S. N. Sarangi, and S. N. Sahu, Appl. Phys. A: Mater. Sci. Process. **86**, 447 (2007).
[13] A. Rogach, S. Kershaw, M. Burt, M. Harrison, A. Kornowski, A. Eychmuller, and H. Weller, Adv. Mater. **11**, 552 (1999).
[14] S. Rath and S. N. Sahu, Europhys. Lett. **67**, 294 (2004).
[15] M. I. D'yakonov and A. V. Khaetskii, JETP Lett. **33**, 110 (1981).
[16] M. I. D'yakonov and A. V. Khaetskii, Sov. Phys. JETP **55**, 917 (1982).
[17] P. C. Sercel, Al. L. Efros, and M. Rosen, Phys. Rev. Lett. **83**, 2394 (1999).
[18] R. Dornhaus and G. Nimtz, Springer Tracts Mod. Phys. **78**, 1 (1976).
[19] G. Bastard, Phys. Rev. B **25**, 7584 (1982).
[20] Y.-C. Chang, J. N. Schulman, G. Bastard, Y. Guldner, and M. Voos, Phys. Rev. B **31**, 2557 (1985).
[21] Y. R. Lin-Liu and L. J. Sham, Phys. Rev. B **32**, 5561 (1985).
[22] N. A. Cade, J. Phys. C **18**, 5135 (1985).
[23] R. A. Suris, Sov. Phys. Semicond. **20**, 1258 (1986).
[24] N. Malkova and U. Ekenberg, Phys. Rev. B **66**, 155325 (2002).
[25] G. M. Minkov, A. V. Germanenko, V. A. Larionova, and O. E. Rut, Phys. Rev. B **54**, 1841 (1996).
[26] B. A. Bernevig, T. L. Hughes, and S.-C. Zhang, Science **314**, 1757 (2006).
[27] M. König, H. Buhmann, L. W. Molenkamp, T. Hughes, C.-X. Liu, X.-L. Qi, and S.-C. Zhang, J. Phys. Soc. Jpn. **77**, 031007 (2008).
[28] Xi Dai, T. L. Hughes, X-L. Qi, Z. Fang, and S.-C. Zhang, Phys. Rev. B **77**, 125319 (2008).
[29] X.-L. Qi, Y.-S. Wu, and S.-C. Zhang, Phys. Rev. B **74**, 085308 (2006).
[30] J. M. Luttinger, Phys. Rev. **102**, 1030 (1956).
[31] G. W. Bryant and W. Jaskólski, Phys. Rev. B **67**, 205320 (2003).
[32] Y. Z. Hu, M. Lindberg, and S. W. Koch, Phys. Rev. B **42**, 1713 (1990).
[33] E. Martin, C. Delerue, G. Allan, and M. Lannoo, Phys. Rev. B **50**, 18258 (1994).
[34] K. Leung and K. B. Whaley, Phys. Rev. B **56**, 7455 (1997).
[35] S. Lee, L. Jonsson, J. W. Wilkins, G. W. Bryant, and G. Klimeck, Phys. Rev. B **63**, 195318 (2001).
[36] G. W. Bryant and W. Jaskólski, J. Phys. Chem. B **109**, 19650 (2005).
[37] G. W. Bryant, J. Comput. Theor. Nanosci. **6**, 1262 (2009).
[38] R. S. Knox, *Solid State Physics* (Academic, New York, 1963), Vol. 5.
[39] L. V. Keldysh, JETP Lett. **29**, 658 (1979).
[40] R. Tsu and D. Babic, Appl. Phys. Lett. **64**, 1806 (1994).
[41] L.-W. Wang and A. Zunger, Phys. Rev. Lett. **73**, 1039 (1994).
[42] C. Delerue, M. Lannoo, and G. Allan, Phys. Rev. B **68**, 115411 (2003).
[43] A. Franceschetti, H. Fu, L. W. Wang, and A. Zunger, Phys. Rev. B **60**, 1819 (1999).
[44] R. Resta, Phys. Rev. B **16**, 2717 (1977).
[45] K. Ohno, Theor. Chim. Acta **2**, 219 (1964).
[46] J. C. Slater, Phys. Rev. **36**, 57 (1930).
[47] F. Herman and S. Skillman, *Atomic Structure Calculations* (Prentice-Hall, New York, 1963).
[48] R. Bauer, D. Bimberg, J. Christen, D. Oertel, D. Mars, J. N. Miller, T. Fukunaka, and H. Nakashima, in *Proceedings of the 18th International Conference on Semiconductor Physics*, Stockholm, 1986, edited by O. Engstrom (World Scientific, Singapore, 1987), p. 525.
[49] Y. Chen, B. Gil, P. Lefebvre, and H. Mathieu, Phys. Rev. B **37**, 6429 (1988).
[50] L. C. Andreani and F. Bassani, Phys. Rev. B **41**, 7536 (1990).
[51] T. Takagahara, Phys. Rev. B **47**, 4569 (1993).